Helmholtz-Zentrum Dresden-Rossendorf (HZDR)

Phase Transitions in C:Ni Nanocomposite Templates during Diameter-Selective CVD Synthesis of SWCNTs

Krause, M.; Melkhanova, S.; Hübner, R.; Haluska, M.; Gemming, S.;

Phase transitions in C:Ni nanocomposite templates during diameter-selective CVD synthesis of SWCNTs

Matthias Krause,[1,*] Svetlana Melkhanova,[1] René Hübner,[1] Miro Haluska,[2] Sibylle Gemming[1,3]

[1] Helmholtz-Zentrum Dresden - Rossendorf, Bautzner Landstaße 400, D-01328 Dresden, Germany

[2] ETH Zürich, Micro and Nanosystems, D-MAVT, CH-8092 Zürich, Switzerland

[3] Technische Universität Chemnitz, D-09107 Chemnitz, Germany

* Corresponding author: Matthias Krause, e-mail: matthias.krause@hzdr.de, Phone: +49 351 2603578

Phase transitions in carbon:nickel nanocomposite templates during CVD synthesis of diameter-controlled SWCNTs were studied. While almost conserving their pre-defined diameter distribution, as-deposited Ni₃C nanoparticles transform into fcc-NiO during activation in low-pressure air atmosphere, and are reduced to a mixture of fcc-Ni and Ni₃C under nanotube growth conditions. The first phase transition leads to a substitutional replacement of the protective carbon matrix by a protective oxide layer. The second one reflects competing reduction processes of NiO. A mechanism for the complementary roles of carbon matrix and Ni species in the three-step CVD synthesis is proposed that includes nanoparticle immobilization, carbon delivery and nanotube growth catalysis.
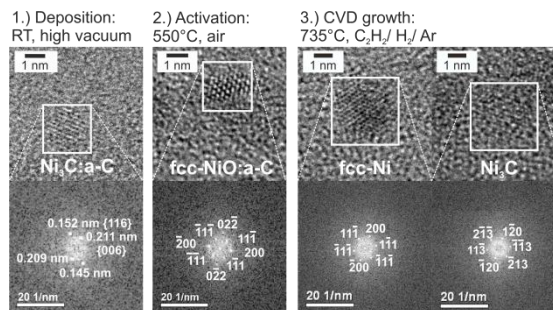
High-resolution TEM micrographs and corresponding FFTs reveal the phase transformations of Ni-rich nanoparticles of C:Ni nanocomposite templates during the steps of the CVD synthesis of diameter-controlled SWCNTs.

1 Introduction

Chirality-selectivity represents a major challenge for single-walled carbon nanotube (SWCNT) application in information technology, microelectronics and medicine [1-4]. Recent improvements towards this goal comprise the enhanced large-scale gel column chromatography separation of SWCNT mixtures [5] or the diameter- and even chirality-selective synthesis [6, 7]. Both approaches have advantages and disadvantages. Among different methods for SWCNT synthesis, catalytic CVD is the most promising one, because it provides high yields, mass-production ability and chirality-selectivity. The latter is caused by lower process temperatures compared to laser ablation and arc discharge.

In CVD growth of SWCNTs, the catalyst properties play a crucial role. Thermally highly-stable synthetic W-Co alloy catalysts were employed to obtain (12,6) tubes with 92%

chiral purity [6]. Predefined catalysts synthesized by physical vapour deposition (PVD) have been more recently used for diameter- and chirality-selective CVD growth of single-walled carbon nanotubes (SWCNTs) [8, 9]. An et al. deposited a 1 nm thin Co-W bilayer by magnetron sputtering, annealing it in air at 400°C and transferred this template into a quartz tube for SWCNT growth at 750°C. The authors reported a (12,6) chirality enrichment of 50-70% [8]. PVD-grown templates circumvent the exhausting optimization of parameters for *in situ* catalyst formation and enable the control of catalyst morphology and microstructure [10]. In our previous work [9], C:Ni nanocomposite templates (NCTs) with pre-defined Ni-rich particles of (2.0±0.3) nm diameter in a carbon matrix were used as catalyst precursors. SWCNTs with a selective, monomodal diameter distribution were obtained by CVD synthesis. More than 50% of the SWCNTs had a diameter of (1.36±0.10) nm. The NCTs

were found to be stable in air and to conserve their morphology to a large extent during the CVD synthesis. The entire process comprised three steps: 1.) PVD deposition of the NCTs at 300°C, 2.) Activation of the NCTs at 550°C in low-pressure flowing air, and 3.) CVD growth of carbon nanotubes at 735°C in low-pressure C_2H_2/ H_2/ Ar atmosphere [9].

While the preparation of NCTs is well defined and controlled [9, 10], the activation of the nanoparticles (NPs) for nanotube growth by CVD is a critical step that is not fully understood yet. In particular, the phase structure of the NPs after the activation step had still to be clarified. Another open question was the reason for the unexpected co-existence of fcc-Ni and Ni_3C after CVD growth of the carbon nanotubes. Atomic force microscopy (AFM), high-resolution transmission electron microscopy (TEM) and Raman spectroscopy were used to complete the knowledge about the phase and microstructure of C:Ni NCTs after the different stages of the SWCNT synthesis. The studies revealed distinct phase changes and transitions of the two NCT components, the catalytically-active NPs and the embedding carbon matrix. The obtained results clarify the mechanisms that are responsible for the conservation of the NP morphology throughout the whole process and point to a complementary role of involved Ni NP species for SWCNT synthesis.

2 Methodologies

2.1 Sample treatment In the first step of sample processing, C:Ni (~15 at.% Ni) NCTs were deposited at 300°C by ion beam co-sputtering of a graphite/Ni zone target onto a Si/SiO₂ (~0.5 µm, thermally oxidized) substrate. The templates are long-term stable in air. In step 2, the NCTs were activated in a CVD oven in low-pressure (2-3 mbar) flowing air at 550°C for 10 minutes. During the subsequent third step, the activated NCTs were exposed to standard conditions for low-pressure CVD growth, notably a C_2H_2/ H_2/ Ar (5/300/300 sccm) gas flow mixture at 735°C and a total pressure of 5.1 mbar for ~20 minutes. A more detailed description of the sample treatment can be found in our previous paper [9].

2.2 Characterization AFM was used to analyse the surface roughness of the NCT samples. AFM imaging was performed in air using a Bruker MultiMode 8 scanning probe microscope operated in ScanAsyst mode with SCANASYST-AIR probes (nominal tip radius 2 nm, maximum tip radius of 12 nm, Bruker). AFM images of 4 x 4 µm² size were recorded with 2048 x 2048 pixels, resulting in a pixel size comparable to the nominal tip radius of 2 nm.

Raman spectra of the sp²-carbon phase after each process step were recorded using a micro-Raman Labram HR spectrometer operated with a 300 lines/mm grating and a liquid nitrogen cooled CCD detector (Horiba-Jobin-Yvon). The laser wavelength of 532 nm was used for excitation, and a 100x magnifying long working distance objective was applied to focus the laser beam. The employed laser power was 1 mW, and no laser-induced graphitization was observed

during the measurements. In order to minimize the contribution of SWCNTs to the Raman spectra after step 3, five sample areas without detectable radial breathing mode (RBM) were measured and the obtained spectra averaged. The detailed analysis of the SWCNT RBM spectra was previously published [9].

Cross-sectional transmission electron micrographs were obtained using an image Cs-corrected Titan 80-300 (FEI) microscope operated at an acceleration voltage of 300 kV. For TEM specimen preparation of the NCT after step 1 the classical procedure described by Bravman and Sinclair was used [11]. For the samples after steps 2 and 3, TEM lamellae were prepared by *in situ* lift-out using a Zeiss Crossbeam NVision 40 system. In each case, a carbon cap layer was deposited to protect the sensitive surface, beginning with electron beam assisted and subsequently followed by Ga focused ion beam (FIB) assisted precursor decomposition. Afterwards, the TEM lamella was prepared using a 30 keV Ga FIB with adapted currents. Its transfer to a 3 post copper lift-out grid (Omniprobe) was done with a Kleindiek micromanipulator. To minimize sidewall damage, Ga ions of only 5 keV energy were used for final thinning of the TEM lamella to electron transparency.

3 Results After process step 1 the NCT is comprised of Ni_3C NPs with a narrow diameter distribution of (2.0±0.3) nm in a carbon matrix (Fig. 1) [9]. The film thickness is the same as the mean NP diameter.
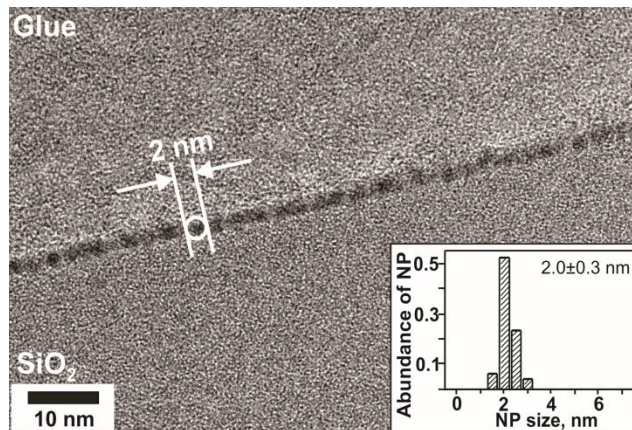
Figure 1 Cross-sectional TEM micrograph of C:Ni NCT after template deposition. The inset displays the NP diameter distribution. The figure is a rearrangement of Fig. 1a) and Fig. 3a) from [9].

The AFM analysis of the NCTs shows an increasing surface roughness from process step 1 via step 2 to step 3 (Fig. 2). The mean height difference after the NCT deposition is (1.0 ± 0.5) nm, i.e. the half of the film thickness. Individual height variations are of the order of 1 nm, with very few 2 nm spikes. No other objects like dirt or dust particles were detected. After step 2, the AFM analysis gave a slightly in-

creased mean height difference of (1.7 ± 0.8) nm. Eventually, after step 3, the height difference distribution covers a range from 0.4 nm to 6.8 nm, with a mean value of (3.2 ± 1.4) nm.
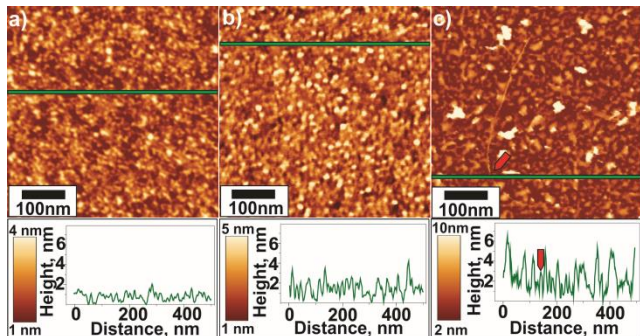
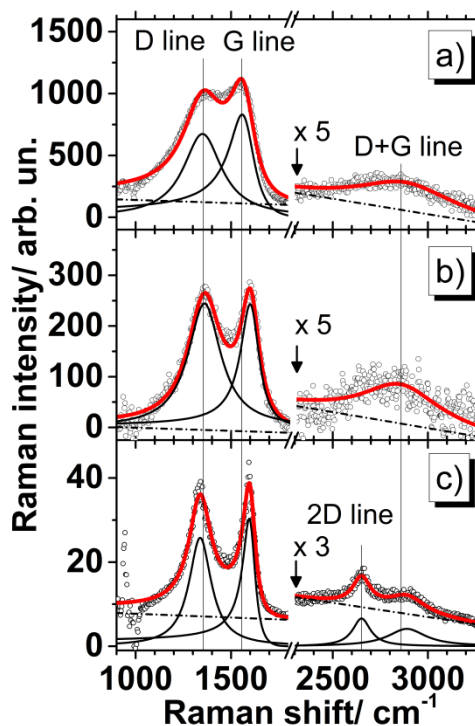**Figure 2** AFM images and height profiles of C:Ni NCTs after different stages of the CVD synthesis of SWCNTs. a) after NCT deposition, b) after NCT activation, c) after nanotube growth. The red arrow in part c) indicates a carbon nanotube.

Even though it would be tempting to correlate the statistics of the height distribution with NP diameters, this is not justified because of the convolution of surface topography with the AFM tip characteristics. For this reason the semi-quantitative conclusion derived from the AFM analysis is that the roughness increase is substantially larger from process step 2 to 3 than from step 1 to step 2. The AFM height profile also includes a SWCNT, which is indicated by an arrow (Fig. 2c). It can be conservatively estimated that its diameter hardly exceeds 2 nm. Obeying the experimental accuracy this is in good agreement with the diameter distribution maximum found by Raman mapping [9].

Beyond the formation of SWCNTs, Raman spectroscopy reveals significant changes of the phase structure of the embedding carbon matrix (Fig. 3). The spectrum after step 1 has the typical characteristics of amorphous sp^2-C (a-C) with broad features corresponding to the D, G, and D+G line (Fig. 3a). Based on the G line position and the I_D/I_G ratio (Table 1), and applying the three-stage-model of Ferrari and Robertson [12], the estimated sp^3-fraction is of the order of 10%. After the activation step, the G line position and I_D/I_G are changed towards the values of nano-crystalline graphite. Since the 2D line is not observed (Fig. 3b), the ordering degree of the sp^2-C phase is still limited. The sp^2-C phase structure can hence be at best described by clustered sixfold sp^2-C rings, whose defect density prevents 2-phonon scattering of K-point phonons [12-14]. Simultaneously to the increased 6-fold ring clustering the integral intensity of the G- and D-line decreased to approximately 20% and 30%, respectively, after process step 2. Since the Raman cross section of carbon increases with its sp^2-fraction, this intensity reduction is attributed to a partial transformation of the embedding carbon matrix into volatile carbon oxides.

Table 1 Raman fit parameter of C:Ni NCTs after the three steps of the synthesis of SWCNTs.

| Raman fit parameter	After NCT deposition	After NCT activation	After SWCNT growth
G line Raman shift (cm^{-1})	1558	1592	1595
D line Raman shift (cm^{-1})	1350	1355	1338
2D line Raman shift (cm^{-1})	-	-	2651
I_D/I_G ratio	0.81	1.00	0.87
I_{2D}/I_G ratio	0	0	0.07

Figure 3 Raman spectra and line shape analysis of C:Ni NCTs after different stages of the CVD synthesis of SWCNTs. a) after NCT deposition, b) after NCT activation, c) after nanotube growth.

As mentioned in the experimental section, five sample areas without detectable RBM were measured and the obtained spectra averaged in order to characterize the supposed non-SWCNT part of the sp^2-C Raman spectrum after process step 3. Nevertheless the Raman shifts of D and 2D line are in very good agreement with those of SWCNTs and significantly lower than in graphite or graphene [15-17]. Since the missing splitting into G^+ and G^- mode can be easily attributed to the low spectral resolution (3 CCD pixels correspond to 9 cm^{-1}) used for these measurements, the observed sp^2-C spectrum is assigned to SWCNTs whose RBM is not in resonance with the exciting laser wavelength. Compared to the initial spectrum after process step 1 the integral

intensity of the G and D line after step 3 is approximately 2%. Since this remaining D and G line intensity is predominantly attributable to SWCNTs, and the Raman cross section of nanotubes is not smaller than that of a-C [18], the major part of a-C remaining after step 2 must have transformed into volatile hydrocarbons during process step 3.

The Ni-rich NPs after process step 1 consist of Ni_3C. After step 3, the FFT analysis of the TEM micrographs showed the coexistence of NPs with fcc- and hcp-Ni lattice [9]. Since hcp-Ni and rhombohedral Ni_3C have the same metal sublattice, the observed hcp-Ni structures were tentatively assigned to Ni_3C NPs. The identification of the phase structure of the Ni-rich NPs after step 2 was open. A high-resolution TEM micrograph of a representative nanocrystal is shown in Fig. 4a.
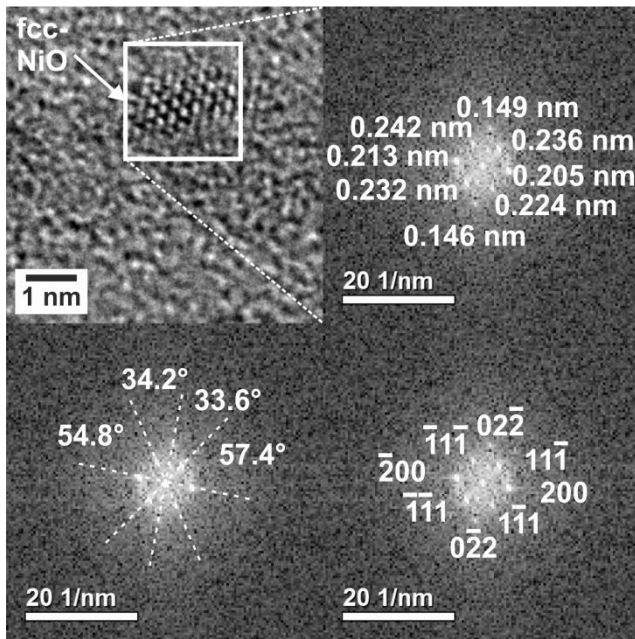
Figure 4 Microstructure analysis of a representative nanocrystal in C:Ni NCTs after activation. a) TEM image, b) FFT with interplanar distances, c) FFT with interplanar angles, d) indexed zone axis pattern.

The FFT analysis of the selected area (Fig. 4a, white square) provides lattice fringe distances (Fig. 4b) and angles (Fig. 4c). Indexing can be done based on a [011] zone axis pattern of an fcc lattice (Fig. 4d). This lattice type is the most stable modification of pure Ni metal as well as of NiO. The comparison of the interplanar distances and angles for the nanocrystal in Fig. 4 with those of fcc-Ni and fcc-NiO (Table 2) shows that the nickel oxide is formed during process step 2. The observed few per cent deviations from bulk crystal values would be usual for nanocrystals, but can be also caused by the inherent accuracy limitations of the FFT analysis of such small objects. In contrast, the lattice plane differences between the nanocrystal and the Ni metal reference

are of the order of 15 to 20% and preclude a phase structure assignment as fcc-Ni.

Table 2 Interplanar distances (d (hkl)) and angles α ((hkl)/(hkl)) of a NiO nanocrystal (nc-NiO) identified after NCT activation (compare Fig. 4) as well as fcc-NiO and fcc-Ni reference structures.

| Lattice parameter	nc-NiO, after NCT activation	fcc-NiO, reference [19]	fcc-Ni, reference [20]
d (111)/ nm	0.234	0.241	0.203
d (200)/ nm	0.209	0.209	0.176
d (220)/ nm	0.148	0.148	0.125
α (111)/(200)/°	56.1	54.7	54.7
α (111)/(220)/°	33.9	35.3	35.3
α (200)/(220)/°	89.0	90.0	90.0

4 Discussion

The presented results have completed the knowledge about phase transitions in C:Ni nanocomposite templates during diameter-controlled SWCNT synthesis. The findings are summarized in Table 3. Based on these results we are able to develop a reaction scenario and to draw conclusions about the catalytically active species for the formation of ordered graphitic carbon.

Table 3 Structural properties of C:Ni NCTs after the steps of the CVD synthesis of SWCNTs.

Structural Properties	After NCT deposition	After NCT activation	After SWCNT growth
Mean NP diameter (nm)	2.0 ± 0.3[9]	2.2 ± 0.4[9]	3.0 ± 0.7[9]
sp^2-carbon phase structure	a-C[this work]	a-C, sp^2-C ring cluster[this work]	SWCNTs[9], [this work]
NP phase structure	rh-Ni_3C, a-Ni_3C[9]	fcc-NiO[this work]	fcc-Ni, rh-Ni_3C[9]

The reactions of the amorphous carbon matrix follow from the Raman data. In step 2, the major a-C fraction transforms into volatile carbon oxides, presumably CO_2. A smaller fraction undergoes an ordering process into sp^2-C six-fold ring clusters, but without measurable graphitic ordering. This observation can be compared to those of a recent study on graphitic ordering on flat Ni surfaces [21]. Therein, graphitic planes oriented horizontally to the Ni surface were formed already at 550°C, i.e. the same temperature as the one used for NCT activation in the present work. Since the metal-rich species within process step 2 are either Ni_3C or NiO, it can be concluded that they are not suitable to catalyse the formation of graphitic carbon under these conditions. During CVD growth, the remaining carbon is transformed as shown and discussed in the Raman section.

The first phase transformation of the Ni-rich NPs in process step 2 is described by equation (1):

$$2\,Ni_3C + 5\,O_2 \rightleftharpoons 6\,NiO + 2\,CO_2 \qquad (1)$$
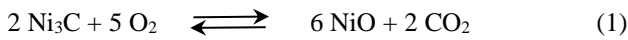
This reaction is thermodynamically favored over the alternative formation of carbon monoxide because of the more than two times larger free formation enthalpy. The reduction of NiO to fcc-Ni in the subsequent step 3 can be described by reaction (2), which is driven by the formation of CO_2 and H_2O:

$$6\,NiO + C_2H_2 + H_2 \rightleftharpoons 6\,Ni + 2\,CO_2 + 2H_2O \qquad (2)$$
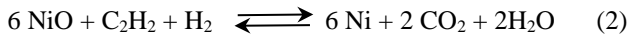
The most surprising structural phase after step 3 was Ni_3C. This compound is metastable and decays into fcc-Ni and carbon at around 400°C even in vacuum [14, 22, 23]. However, at reducing conditions as represented by C_2H_2/H_2 in the CVD growth step, a disproportionation of the acetylene carbon according to equation (3) accounts for the formation of Ni_3C:

$$3\,NiO + C_2H_2 + H_2 \rightleftharpoons Ni_3C + CO + 2H_2O \qquad (3)$$
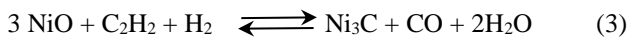
The proposed reactions of NiO with C_2H_2/H_2 are supported by thermodynamic data and literature results. The free standard reaction enthalpies of equations (2) and (3) are of the order of -140 kJ/ mol and -120 kJ/ mol, respectively [24, 25]. These values will change only by 10 to 20 % at 735°C. Hence, the reactions (2) and (3) are thermodynamically spontaneous at the temperature of CVD growth in this work. In the literature it was shown that acetylene is transformed into carbon oxides and Ni by 100%, if it is exposed to NiO nanoparticles [26]. The partial pressure ratio of the resulting CO/ CO_2 mixture was 43.2 at 1100 K [26], about two to three times higher than the corresponding ratio of the Boudouard equilibrium at this temperature. The increased amount of CO compared to CO_2 points to the occurrence of both reactions. One more support for reaction (3) is the observed CO formation when C_2H_2 adsorbed at Ni(111)/ O(2x2) was heated to around 325°C [27].

Environmentally driven restructuring of catalyst nanoparticles was formerly observed e.g. for Rh-Pd core-shell particles and Rd-Pd bilayers [28-30]. While the Pd metal formed the shells in reducing conditions because of its lower surface energy, the sequence inverted in oxidizing environment because of the higher formation enthalpy of RhO [28, 29]. Similar stacking sequence changes were found in Rh-Pd bilayers when the atmosphere was switched between CO and NO [30].

For a principal understanding of the underlying mechanisms of the reactions (2) and (3), the surface chemistry of acetylene, C_2H_2, on NiO and Ni shall be briefly reviewed. Two adsorbate complexes were identified in these systems by photoemission spectroscopy: i) π-bonded acetylene on clean Ni(111) surfaces, and ii) CH species at Ni(111)/ O(2x2) and NiO(111) [27]. Later on, π-bonded acetylide-Ni complexes were found as another acetylene-derived species

on Ni surfaces [31]. These surface species undergo thermally-induced decomposition of into hydrogen and precipitated carbon at temperatures above 200°C [27, 31, 32]. Summarizing the presented experimental results and the discussion so far, different forms of carbon as well as of acetylene may act as potential carbon sources for the formation of SWCNTs in process step 3. They can be specified as follows:

a) Remaining a-C in the C:Ni NC templates,
b) Ni_3C and dissolved carbon in Ni,
c) Precipitated carbon resulting from decomposed acetylene-derived adsorbates,
d) Acetylene-derived hydrocarbon surface species.

Acetylene and its surface species are generally accepted as sources for SWCNT growth [33]. The experimental evidence, whether a) and b) are also relevant for SWCNT growth could be provided by additional experiments exposing the C:Ni NCTs after step 2 to hydrogen. Moreover, isotope labelling of the acetylene would be helpful to further resolve the carbon source responsible for nanotube growth.

It is an interesting question, whether the coexistence of fcc-Ni and rhombohedral Ni_3C after CVD allows conclusions about synergetic or complementary roles of both species for SWCNT formation. In agreement with Bayer et al. [23], no graphitic ordering was observed after NCT deposition at 300°C, when Ni exists in the form of Ni_3C. However, different to their conditions, Ni_3C was re-formed during SWCNT growth. The dynamic equilibrium between fcc-Ni, dissolved C in fcc-Ni and Ni_3C, proposed by Bayer et al. for the decay of Ni_3C [23], could be reversed under growth conditions used in the present study, as indicated in equation (4):

$$3\,fcc\text{-}Ni + C \rightleftharpoons 3\,fcc\text{-}Ni(\text{-}1/3\,I_C) \rightleftharpoons Ni_3C \qquad (4).$$
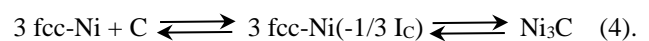
The middle species fcc-Ni(-1/3) represents fcc-Ni with dissolved carbon at Ni interstitials (I_C). Under such reaction conditions the fcc-Ni could be the catalytically active site, and the other species would provide the atomic carbon for further SWCNT growth.

5 Conclusions

C:Ni nanocomposite templates undergo a series of phase transitions during diameter-selective CVD synthesis of SWCNTs. The template components take different roles in this process. The initial diameter of the Ni_3C NPs is controlled by the deposition process, and the embedding a-C matrix is responsible for NP immobilization and protection. During template activation, the NPs are getting self-protected by their transformation into NiO. In the nanotube growth step, the NP phase structure results from competing reduction processes of NiO. It is proposed that a dynamic

equilibrium of fcc-Ni and Ni_3C enables catalysis and carbon delivery. The advantages of the catalyst embedded in a-C matrix are their size defined preparation and the particle size "conservation" by preventing Ostwald ripening and nano-particle agglomeration prior to nanotube growth. Optimizing the time regime of the growth step might be a promising way to further improve the diameter-selectivity of C:Ni NCTs catalysts for SWCNT growth [34].

References

[1] H. Wang, Y. Yuan, L. Wei, K. Goh, D. S. Yu and Y. Chen, Carbon 81, 1-19 (2015).

[2] M. F. L. De Volder, S. H. Tawfick, R. H. Baughman and A. J. Hart, Science 339 (6119), 535-539 (2013).

[3] A. Kaskela, P. Laiho, N. Fukaya, K. Mustonen, T. Susi, H. Jiang, N. Houbenov, Y. Ohno and E. I. Kauppinen, Carbon 103, 228-234 (2016).

[4] S. Vollebregt and R. Ishihara, Carbon 96, 332-338 (2016).

[5] Y. Yomogida, T. Tanaka, M. F. Zhang, M. Yudasaka, X. J. Wei and H. Kataura, Nature Communications 7 (2016).

[6] F. Yang, X. Wang, D. Zhang, J. Yang, LuoDa, Z. Xu, J. Wei, J.-Q. Wang, Z. Xu, F. Peng, X. Li, R. Li, Y. Li, M. Li, X. Bai, F. Ding and Y. Li, Nature 510 (7506), 522-524 (2014).

[7] J. R. Sanchez-Valencia, T. Dienel, O. Groning, I. Shorubalko, A. Mueller, M. Jansen, K. Amsharov, P. Ruffieux and R. Fasel, Nature 512 (7512), 61-64 (2014).

[8] H. An, A. Kumamoto, H. Takezaki, S. Ohyama, Y. Qian, T. Inoue, Y. Ikuhara, S. Chiashi, R. Xiang and S. Maruyama, Nanoscale 8 (30), 14523-14529 (2016).

[9] S. Melkhanova, M. Haluska, R. Hübner, T. Kunze, A. Keller, G. Abrasonis, S. Gemming and M. Krause, Nanoscale 8 (31), 14888-14897 (2016).

[10] M. Krause, A. Mücklich, T.W.H. Oates, M. Zschornack, S. Wintz, J.L. Endrino, A. Shalimov, S. Gemming, G. Abrasonis, Applied Physics Letters 101, 053112 (2012)

[11] J. C. Bravman and R. Sinclair, Journal of Electron Microscopy Technique 1 (1), 53-61 (1984).

[12] A. C. Ferrari and J. Robertson, Physical Review B 61 (20), 14095-14107 (2000).

[13] S. Reich and C. Thomsen, Philosophical Transactions of the Royal Society a-Mathematical Physical and Engineering Sciences 362 (1824), 2271-2288 (2004).

[14] G. Abrasonis, M. Krause, A. Mücklich, K. Sedlacˇková, G. Radnóczi, U. Kreissig, A. Kolitsch and W. Möller, Carbon 45 (15), 2995-3006 (2007).

[15] J. Maultzsch, S. Reich and C. Thomsen, Physical Review B 64 (12) (2001).

[16] F. Simon, V. Zolyomi, R. Pfeiffer, H. Kuzmany, J. Koltai and J. Kurti, Physical Review B 81 (12) (2010).

[17] P. T. Araujo, M. Terrones and M. S. Dresselhaus, Materials Today 15 (3), 98-109 (2012).

[18] J. E. Bohn, P. G. Etchegoin, E. C. Le Ru, R. Xiang, S. Chiashi and S. Maruyama, Acs Nano 4 (6), 3466-3470 (2010).

[19] G. M. K. Martin, in ICDD pattern volume card 00-047-1049 (International Center of Diffraction Data, 1991).

[20] T. Swanson, in ICDD pattern 00-004-0850 (International Center of Diffraction Data, 1953).

[21] R. Wenisch, R. Hübner, F. Munnik, S. Melkhanova, S. Gemming, G. Abrasonis and M. Krause, Carbon 100, 656-663 (2016).

[22] T. B. Massalski, Binary alloy phase diagrams. (ASM International, Metals Park, Ohio, 1991).

[23] B. C. Bayer, D. A. Bosworth, F. B. Michaelis, R. Blume, G. Habler, R. Abart, R. S. Weatherup, P. R. Kidambi, J. J. Baumberg, A. Knop-Gericke, R. Schloegl, C. Baehtz, Z. H. Barber, J. C. Meyer and S. Hofmann, Journal of Physical Chemistry C 120 (39), 22571-22584 (2016).

[24] J. A. Manion, Journal of Physical and Chemical Reference Data 31 (1), 123-172 (2002)

[25] D'Ans, Lax, Taschenbuch für Chemiker und Physiker, Band III: Elemente, anorganische Verbindungen und Materialien, Minerale. (Springer Berlin Heidelberg, 1998).

[26] N. B. Poddar, S. Thomas, F. S. Ehrenhauser and M. J. Wornat, Proceedings of the Combustion Institute 32, 1847-1854 (2009).

[27] J. E. Demuth, Surface Science 69 (2), 365-384 (1977).

[28] F. Tao, M. E. Grass, Y. W. Zhang, D. R. Butcher, J. R. Renzas, Z. Liu, J. Y. Chung, B. S. Mun, M. Salmeron and G. A. Somorjai, Science **322** (5903), 932-934 (2008).

[29] F. Tao, M. E. Grass, Y. W. Zhang, D. R. Butcher, F. Aksoy, S. Aloni, V. Altoe, S. Alayoglu, J. R. Renzas, C. K. Tsung, Z. W. Zhu, Z. Liu, M. Salmeron and G. A. Somorjai, Journal of the American Chemical Society **132** (25), 8697-8703 (2010).

[30] G. Abrasonis, S. Wintz, M. O. Liedke, F. A. Akgul, M. Krause, K. Kuepper, D. Banerjee, Z. Liu and S. Gemming, Journal of Physical Chemistry C **116** (27), 14401-14407 (2012).

[31] L. Vattuone, Y. Y. Yeo, R. Kose and D. A. King, Surface Science **447** (1-3), 1-14 (2000).

[32] J. E. Demuth and D. E. Eastman, Physical Review Letters **32** (20), 1123-1127 (1974).

[33] C. T. Wirth, C. Zhang, G. F. Zhong, S. Hofmann and J. Robertson, Acs Nano **3** (11), 3560-3566 (2009).

[34] H. Navas, M. Picher, A. Andrieux-Ledier, F. Fossard, T. Michel, A. Kozawa, T. Maruyama, E. Anglaret, A. Loiseau and V. Jourdain, Acs Nano **11** (3), 3081-3088 (2017).